EXPERIMENTAL AND ANALYTICAL STUDY ON FLUID WHIRL AND FLUID WHIP MODES

Agnes Muszynska
Bently Rotor Dynamics Research Corporation
Minden, Nevada

ABSTRACT

Fluid whirl and fluid whip are rotor self–excited, lateral vibrations which occur due to rotor interactions with the surrounding fluid. There exist various modes of fluid whirl and fluid whip. These modes are close to rotor modes corresponding to free vibrations (based on the linear model). Small differences are due to nonlinearities in the system. This paper presents experimental and analytical results on the lowest modes of fluid whirl and fluid whip. Examples of rotors supported in fluid lubricated bearings show the variations of rotor deflection amplitudes and phases in the whirl and whip modes with changes of rotative speeds and/or changes in lumped mass locations along the shaft.

1. INTRODUCTION

Dynamic phenomena induced by interaction between the rotor and the surrounding fluid, such as occur in fluid–lubricated bearings and seals of fluid–handling machines, have been recognized for over 60 years. The resulting rotor lateral self–excited vibrations, usually occurring at subsynchronous frequencies, are known as "fluid (oil,..) whirl, "fluid (aerodynamic, steam,..) whip," or simply "rotor instability." The rotor precessional direction of these self–excited vibrations is always forward. Most of the existing literature have documented occurrences of these phenomena in low ranges of rotative speeds [1–6]. Classical literature on fluid–lubricated bearings, which concentrates on lubrication problems rather than rotor instabilities, reports only occurrences of whirl vibrations of rigid rotors. References on rotor instability due to dynamic phenomena occurring in seals report whip type of vibrations only. This leads to an unjustified belief that the whirl and whip phenomena may occur only in dissimilar, uncomparable systems, and are due to different causes.

When the rotating shaft and surrounding fluid involved in motion are considered, however, as one system, it is evident that vibration modes interact. If the fluid–induced, self–excited vibrations of the rotor occur at relatively low rotative speed, the shaft would vibrate as either rigid body (whirl), or at its first lateral mode [7]. With an increase in rotative speed, there is a smooth transition from the whirl to whip of the first mode. It is obvious that both these phenomena are generated by the same source, and thus can be modeled by one algorithm. At higher rotative speed, higher mode whirl or whip vibrations may be induced [8,9]. The modal approach in rotor system modeling allows for clear interpretation of the occurring vibrational phenomena.

This paper is a continuation of the series of papers [7–11] on applications of the improved model of the fluid force for lightly radially loaded shafts rotating in a fluid environment. Following Bolotin [12] and Black [13,14], the fluid force model is based on the strength of the circumferential flow generated mainly by the shaft rotation [15]. This model can be used for lightly radially loaded bearings, as well as seals (with or without preswirls and/or injections). The fluid force model, identified experimentally by using physical perturbation techniques [16,17] and the modal approach in modeling, allow for more adequate prediction of rotor stability

thresholds, and evaluation of the post–stability fluid–induced rotor lateral limit cycle self–excited vibration parameters (whirl and whip).

Using the multi–mode modal approach [8, 17], the linearized rotor system eigenvalue problem is solved, and approximate values of natural frequencies and thresholds of stability are given. It is shown that there exist fluid–generated natural frequencies of the system, and the corresponding sequence of modes. The nonlinear model allows for calculation of the after–threshold, self–excited vibration parameters, including modes of vibration.

2. MATHEMATICAL MODEL OF A TWO–MODE ROTOR WITH ONE SOURCE OF INSTABILITY

Two physical models of rotors on which mathematical models are the same will be discussed in this section. In both cases the rotors carry one source of fluid–induced instability.

Consider a balanced isotropic rotor of a fluid–handling machine supported by two rigid bearings. The rotor rotates concentrically in a seal located at the axial section "S" (Fig. 1a). Consider a balanced isotropic rotor rotating concentrically in one fluid–lubricated and one rigid bearing (Fig. 1b). When using the multi–mode modal approach (mode summation), the mathematical model of the rotor, in both cases, is as follows:

$$
\begin{aligned}
&M_1\ddot{z}_1 + D_1\dot{z}_1 + (K_1+K_2)z_1 - K_2z_2 = 0\\
&M_2\ddot{z}_2 + D_2\dot{z}_2 + (K_2+K_3)z_2 - K_2z_1 - K_3z_3 = 0\\
&D(\dot{z}_3 - j\lambda\Omega z_3) + (K_B+K_3+K_4)z_3 + z_3\psi(|z_3|) - K_3z_2 = 0\\
&z_i(t) = x_i(t) + jy_i(t), \quad i=1,2,3, \quad |z_3| = \sqrt{x_3^2 + y_3^2}, \quad j=\sqrt{-1}, \quad \cdot = d/dt
\end{aligned}
\tag{1}
$$

where x_i, y_i are rotor horizontal and vertical displacements, M_1, M_2, K_1, K_2, K_3, K_4, D_1, D_2 are two–mode rotor modal masses, stiffnesses, and external damping coefficients, respectively (in case of the fluid–lubricated bearing, the stiffness K_4 either equals zero or represents an external supporting spring (Fig. 1b)). D, K_B, λ are seal or bearing fluid radial damping, radial stiffness and circumferential average velocity ratio, respectively, ψ is fluid nonlinear stiffness function of radial displacement, Ω is rotative speed, t is time.

For clarity of presentation, the unbalance forces, radial side–load forces, external cross damping, fluid inertia effect, and other nonlinear functions are omitted in the model.

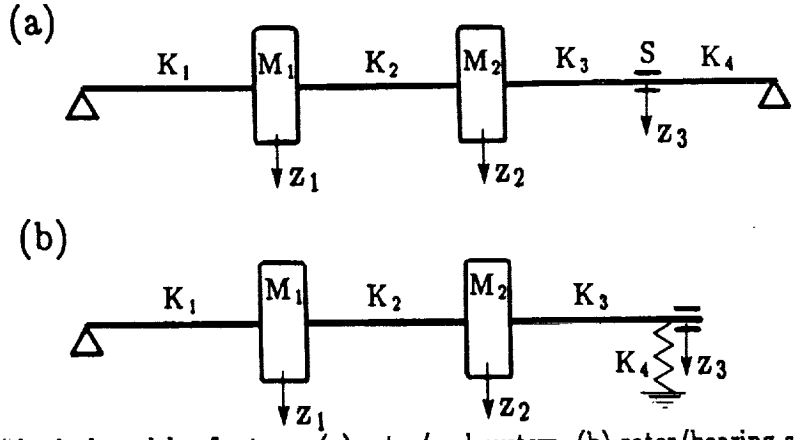

Fig. 1 Physical models of rotors: (a) rotor/seal system, (b) rotor/bearing system.

2.1 Eigenvalue Problem: Natural Frequencies, Thresholds of Stability

The eigenvalue problem for the linearized Eqs. (1) (that is, when ψ=0) provides the following characteristic equation:

$$(\bar{\kappa}_1\bar{\kappa}_2-K_3^2)[jD(\omega-\lambda\Omega) + K_B + K_3 + K_4] - K_3^2\bar{\kappa}_1 = 0 \tag{2}$$

where

$$\bar{\kappa}_i = K_i + K_{i+1} + j\omega D_i - M_i\omega^2, \quad i=1,2 \tag{3}$$

are rotor partial complex dynamic stiffnesses and ω is the complex eigenvalue. Eq. (2) can certainly be solved numerically for specific parameter values. It is the author's intention, however, to show specific qualitative features of this equation solution.

The split of Eq. (2) into real and imaginary parts provides the following equations:

$$D\omega(\omega-\lambda\Omega)(\kappa_1D_2+\kappa_2D_1) - (\kappa_1\kappa_2-K_3^2-\omega^2D_1D_2)(K_B+K_3+K_4) + K_3^2\kappa_1 = 0 \tag{4}$$

$$D(\omega-\lambda\Omega)(\kappa_1\kappa_2-K_3^2-\omega^2D_1D_2) + \omega(\kappa_1D_2+\kappa_2D_1)(K_B+K_3+K_4) - K_3^2\omega D_1 = 0 \tag{5}$$

where κ_1, κ_2 are direct dynamic stiffnesses, that is the real parts of the complex dynamic stiffnesses (3). The approximate values of the system natural frequencies (real parts of ω) can be calculated from Eq. (5). With damping D_i assumed of the second order of smallness the zero–th approximation establishes $\omega_1 \approx \lambda\Omega$, $\omega_{2,\ldots,5} \approx \pm\omega_{ni}$, i=1,2. The first approximation provides more accurate relationships:

$$\text{FLUID WHIRL FREQUENCY} \equiv \omega_1 \approx \lambda\Omega \left[1 - \right.$$

$$\left. - D_1 \frac{[K_2+K_3-M_2\lambda^2\Omega^2+(K_1+K_2-M_1\lambda^2\Omega^2)D_2/D_1](K_B+K_3+K_4)-K_3^2}{D[(K_1+K_2-M_1\lambda^2\Omega^2)(K_2+K_3-M_2\lambda^2\Omega^2) - K_3^2 - \lambda^2\Omega^2D_1D_2]}\right] \tag{6}$$

$$\text{FLUID WHIP FREQUENCIES} = \omega_{2,3} \approx \omega_{ni} -$$

$$- (-1)^iD_1 \frac{[K_2+K_3-M_2\omega_{ni}^2+(K_1+K_2-M_1\omega_{ni}^2)D_2/D_1](K_B+K_3+K_4)-K_3^2}{2D(\omega_{ni}-\lambda\Omega)M_1M_2(\omega_{n2}^2-\omega_{n1}^2)}, \quad i=1,2 \tag{7}$$

$$\text{REVERSE MODE FREQUENCIES} = \omega_{4,5} \approx -\omega_{n1,n2} \tag{8}$$

where ω_{n1}, ω_{n2} are solutions of the rotor partial characteristic equation $\kappa_1\kappa_2 - K_3^2 = 0$:

$$\omega_{ni} = \left\{\frac{K_1+K_2}{2M_1} + \frac{K_2+K_3}{2M_2} + (-1)^i\sqrt{\left[\frac{K_1+K_2}{2M_1} - \frac{K_2+K_3}{2M_2}\right]^2 + \frac{K_3^2}{M_1M_2}}\right\}^{1/2}, \quad i=1,2 \tag{9}$$

The approximation (7) cannot be applied for the value $\Omega=\omega_{ni}/\lambda$, thus this case should be calculated using Eq. (6).

The fluid whirl frequency ω_1 is almost a linear function of the rotative speed. The fluid whip frequencies $\omega_{2,3}$ are independent from the rotative speed. At the crossing of ω_1 with ω_2 and ω_3

in the plane (Ω, ω_i), i=1,2,3, the straight lines degenerate into hyperbolas (Fig. 2), resulting in a smooth transitions from the whirl—to—whip and whip—to—whirl modes.

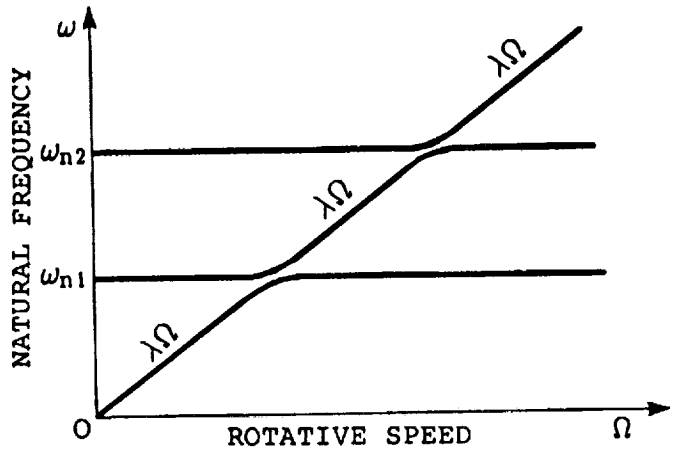

Fig. 2 Natural frequencies versus rotative speed.

Eq. (4) provides the approximate values for stability thresholds. For the whirl onset, ω in Eq. (4) is substituted by $\lambda\Omega_{ST}$ (the zero—th approximation (6) with $D_1=D_2=0$). The resulting quadratic equation for Ω_{ST}^2 establishes:

$$\Omega_{ST\,i} = \frac{1}{\lambda}\left\{\frac{K_1+K_2}{2M_1} + \frac{K_2}{2M_2} + \frac{K_3(K_B+K_4)}{2M_2(K_3+K_B+K_4)} + \right.$$

$$\left. + (-1)^i \sqrt{\left[\frac{K_1+K_2}{2M_1} - \frac{K_2}{2M_2} - \frac{K_3(K_B+K_4)}{2M_2(K_3+K_B+K_4)}\right]^2 + \frac{K_2^2}{M_1 M_2}}\right\}^{1/2}, \qquad i=1,2 \quad (10)$$

There exist, therefore, two instability onsets leading to the fluid whirl instability. For the whip cessations, ω in Eq. (4) is substituted by ω_{ni}, i=1,2 (the zero—th approximation (7) with $D_1 = D_2 = 0$), and Ω is substituted by $\Omega_{ST\,i+2}$:

$$\Omega_{ST\,i+2} = \frac{1}{\lambda}\left\{\omega_{ni} + \frac{K_2^2}{D\omega_{ni}[D_2+D_1(K_2+K_3-M_2\omega_{ni}^2)^2/K_2^2]}\right\}, \qquad i=1,2 \qquad (11)$$

Note that all stability thresholds are inversely proportional to the fluid circumferential velocity ratio λ. The onsets (10) do not depend on damping, while the cessations (11) do: larger damping, lowers the cessation rotative speed, thus narrowing the range where the instability occurs. Practically, the cessations seldom occur at rotative speeds (11), because the rotor is already in the self—excited vibration condition, and the system parameters differ from the linear ones. (The first order approximation (11) does not show dependence on K_B, thus no dependence on ψ; it is necessary to consider higher approximations).

In the rotor/seal system case, the fluid radial stiffness K_B is usually smaller than the stiffness K_4, thus the third term in Eq. (10), and the third term under the radical in Eq. (10), are approximately the stiffnesses of the rotor right portion, combined by two elements in sequence: $K_3K_4/(K_3+K_4)$ (Fig. 1a). The expressions in large parentheses of Eq. (10) represent, therefore,

the natural frequencies of the entire shaft. The stability onset expressed as the $1/\lambda$ fraction of the natural frequency (which for the most often used value λ=0.5 equals 2) is well known in rotor/seal dynamics. At the rotative speed as high as double the first natural frequency, only whip type of instability may occur. That is why very often only whip, and no whirl vibrations, are associated to rotor/seal dynamics. As Eq. (10) indicates, however, the multiplier $1/\lambda$ is not necessarily equal to 2 (which it very seldom is), but depends on the actual circumferential flow conditions in the seal. Swirl brakes or anti–swirl injections can significantly modify λ [11]. Additionally, the fluid radial stiffness may modify the instability onset (10): the larger K_B, the higher the instability onset. (A larger fluid radial stiffness results, for instance, from a higher external pressure of the fluid.) The onset (10) also depends on the location of the seal along the rotor, thus on the values of stiffnesses K_3 and K_4.* The highest values of the onsets (10) occur where the stiffness K_3 is equal to $K_B + K_4$, that is, when the seal is located approximately in the middle between the second modal mass and the right–side bearing.

The function $f_1 = \kappa_1\kappa_2 - K_{\frac{1}{2}}^2$, which provides the whip frequencies ω_{ni}, Eq. (9), and the functions $f_2 = (\kappa_1\kappa_2 - K_{\frac{1}{2}}^2)/\kappa_1$, $f_3 = K_{\frac{3}{4}}^2/(K_B+K_3+K_4)$, which provide onsets of instability, Eq. (10), can be investigated graphically in the plane (ω^2, f_ν), ν=1,2,3. The result is presented in Figure 3. The instability onsets can be found on intersections of the hyperbola f_2 and the straight line f_3 . Now it is easy to discuss the effect of the stiffnesses K_3, K_4, K_B on the instability onsets. If the stiffness K_4 is low (rotor/bearing model), then the line f_3 is higher, and the resulting stability onsets occur at lower rotative speeds, thus, very often in the whirl instability range. An increase of the stiffness K_3 (mass M_2 closer to the instability source) results, again, in a decrease of the instability onset. An increase of the fluid radial stiffness K_B provides a stability improvement by moving the instability onsets toward higher rotative speeds. In all cases, however, the onsets occur at the speeds $\Omega_{ST\,i}$ which are lower than ω_{ni}/λ, i=1,2.

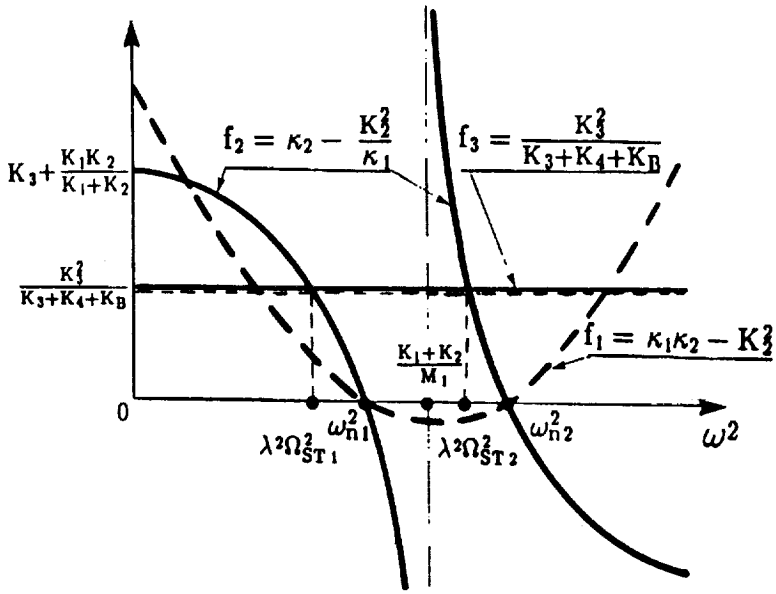

Fig. 3 Graphical solution of Eqs. (4) and (5) showing whip frequencies (9) and onsets of instability (10).

*In this study the seal location is chosen outside the modal masses; a similar analysis can be performed for a case where the seal is located between the modal masses, that is being closer to the second mode nodal point.

2.2 Rotor Modes

The complex modal functions that are calculated from the linear part of Eqs. (1) are as follows:

$$\bar{\phi}_{1\nu} = 1, \quad \bar{\phi}_{2\nu} = 1 + \frac{K_1+D_1 j\,\omega-M_1\omega^2}{K_2}, \quad \bar{\phi}_{3\nu} = \frac{K_3(K_1+K_2+D_1 j\,\omega-M_1\omega^2)}{K_2[Dj(\omega-\lambda\Omega)+K_B+K_3+K_4]} \tag{12}$$

Using the natural frequencies (6) and (7), the approximate modal functions at stability thresholds are obtained. The modal functions of the first and second mode whirls are as follows:

$$\bar{\phi}_{1i} = 1, \quad \bar{\phi}_{2i} \approx \xi - (-1)^i \sqrt{\xi^2 + \frac{M_1}{M_2}}, \quad \bar{\phi}_{3i} \approx \bar{\phi}_{2i} \frac{K_3}{K_B+K_3+K_4}, \quad i=1,2 \tag{13}$$

where

$$\xi = \frac{1}{2}\left[\frac{K_1}{K_2} + 1 - \frac{M_1}{M_2} - \frac{K_3M_1(K_B+K_4)}{K_2M_2(K_B+K_3+K_4)}\right]$$

The modal functions of the first and second mode whips are as follows:

$$\bar{\phi}_{1i+2} = 1, \qquad \bar{\phi}_{2i+2} \approx 1 + \frac{K_1 - M_1\omega_{ni}^2}{K_2},$$

$$\bar{\phi}_{3i+2} \approx \frac{\bar{\phi}_{2i+2}K_3}{\sqrt{(K_B+K_3+K_4)^2 + D^2(\omega_{ni}-\lambda\Omega_{ST\,i+2})^2}} e^{-j\frac{D(\omega_{n\,i}-\lambda\Omega_{ST\,i+2})}{K_B+K_3+K_4}}, \quad i=1,2 \tag{14}$$

where ω_{ni} are given by Eq. (7) and $\Omega_{ST\,i+2}$ by Eq. (11).

During the whirl of the first mode, the entire shaft vibrates in phase. During the second mode whirl, the modal masses M_1, M_2 are 180° out of phase (when damping is neglected). During the first and second mode whips, two rotor masses vibrate in phase, and 180° out of phase, respectively, but the seal location leads the vibration of the second mass by an angle which depends on the system parameters (Eq. (14)).

2.3 Self–Excited Vibrations

After the onsets of instability, the rotor self–excited vibrations occur. Eqs. (1) have exact periodic solutions of the circular form:

$$z_1 = A_1 e^{j(\omega t+\alpha_1)}, \quad z_2 = A_2 e^{j(\omega t+\alpha_2)}, \quad z_3 = A_3 e^{j\omega t} \tag{15}$$

with frequency (or frequencies) ω, and corresponding amplitudes A_i, and phases α_i, i=1,2 relative to the phase of the fluid instability source location. Eqs. (15) describe rotor self–excited vibrations, known as whirl and whip. They occur as steady–state limit cycles after the onsets of instability and some transient process.

The frequencies, amplitudes, and phases of Eqs. (15) can be calculated from the set of nonlinear algebraic equations obtained by substituting (15) into Eqs. (1), and dividing all terms by $e^{j\omega t}$.

Note that the argument of the only nonlinear function ψ becomes now A_3. The final algebraic equations are as follows:

$$A_3 = \psi^{-1}\left[\frac{K_3^2\omega D_1 - D(\omega-\lambda\Omega)(\kappa_1\kappa_2 - K_3^2 - \omega^2 D_1 D_2)}{\omega(\kappa_1 D_2 + \kappa_2 D_1)} - K_B - K_3 - K_4\right] \tag{16}$$

$$A_1 e^{j\alpha_1} = \frac{K_2 K_3}{\bar{\kappa}_1\bar{\kappa}_2 - K_2^2} A_3 , \qquad A_2 e^{j\alpha_2} = \frac{K_3\bar{\kappa}_1}{\bar{\kappa}_1\bar{\kappa}_2 - K_2^2} A_3 \tag{17}$$

where $\bar{\kappa}_i$, κ_i, i=1,2 are dynamic stiffnesses (3) and their real parts, respectively, and ψ^{-1} denotes the inverse function ψ. The frequency ω in Eq. (16) should be substituted by the frequencies obtained from the equation which differs from the characteristic equation (2) only by one nonlinear term. The approximate values for the self–excited vibration frequencies are, therefore, very close to the fluid whirl and whip frequencies. In Eqs. (6) and (7) the fluid radial stiffness K_B should read $[K_B+\psi(A)]$. Since the second terms in Eqs. (6) and (7) are proportional to rotor damping, and thus are relatively small, the above–discussed nonlinear function adjustment will, therefore, bring very little change to the approximate frequencies (6), (7). The reverse mode frequencies (8) do not satisfy Eq. (16).

For the whip frequencies $\omega = \omega_{n1}$ or $\omega = \omega_{n2}$, the denominators of Eqs. (17) are controlled only by damping, thus, independently of the amplitude A_3, the rotor with masses M_1, M_2 is in "resonant" conditions corresponding to its two lateral modes.

It is easy to show that for the first mode whirl and whip frequencies, the phase angles α_1 and α_2 are negative, thus the mass locations are lagging the instability source at the bearing or seal. For the second mode, the phase lag also occurs additionally to the relative 180° phase change of the modal mass locations. The instability source phase leading of the whirl or whip vibrations is well recognized in the field, and has become the basis of the identification method for the instability source axial location on machinery trains [18].

3. MULTI–MODE ROTOR WITH ONE SOURCE OF INSTABILITY

An analysis similar to that presented in the previous chapter can be performed for the multi–mode rotor (Fig. 4). The rotor characteristic equation now has the following form:

$$[Dj(\omega-\lambda\Omega) + K_B + K_{n-1} + K_n]\bar{\kappa} - K_{n-1}^2 = 0 \tag{18}$$

where

$$\bar{\kappa} = \left\{ \bar{\kappa}_{n-2} - \cfrac{K_{n-2}^2}{\bar{\kappa}_{n-3} - \cfrac{K_{n-3}^2}{\bar{\kappa}_{n-4} - \cfrac{K_{n-4}^2}{\bar{\kappa}_{n-5} - \cfrac{\ddots}{\bar{\kappa}_4 - \cfrac{K_4^2}{\bar{\kappa}_3 - \cfrac{K_3^2}{\bar{\kappa}_2 - \cfrac{K_2^2}{\bar{\kappa}_1}}}}}}} \right\}$$

and

$$\bar{\kappa}_i = K_i + K_{i+1} + j\omega D_i - M_i\omega^2, \qquad i=1,...,n-2$$

are rotor partial complex dynamic stiffnesses. The stiffness $\bar{\kappa}$ represents the dynamic stiffness of the rotor, except its last section at the right side (Fig. 4). The real part of $\bar{\kappa}$, when equalized to zero, will provide the zero—th approximation to whip frequencies $\omega \approx \omega_{ni}$, i=1,...,n—2.

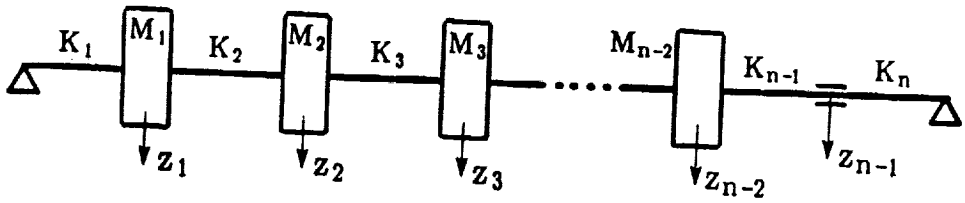

Fig. 4 Multi—mode rotor/bearing/seal model.

The zero—th approximation to the whirl frequency is still $\omega \approx \lambda\Omega$. The further terms in approximations to whirl and whip frequencies, which can be calculated from the imaginary part of Eq. (18), are proportional to the external damping, and except for the regions when $\Omega = \omega_{ni}/\lambda$, they are small.

Similarly to Eq. (4), the real part of Eq. (18) provides the stability thresholds.

The corresponding graphical analysis that is discussed in Section 2.1 can also be performed for Eq. (18). The result indicates virtually the same features: the instability onsets occur at rotative speeds lower than $1/\lambda$ fraction of natural frequencies, and can be controlled by the similar parameters, namely, λ, K_{n-1}, K_n, and K_B.

4. EXPERIMENTAL RESULTS

4.1 Experimental Rig

The experimental rotor, which was made of steel, consisted of a 0.375" diameter shaft with two disks of the mass 4.637×10^{-3} lb.s^2/in (inboard) and 4.643×10^{-3} lb.s^2/in (outboard). The rotor was supported inboard by a relatively rigid sliding bearing bushing, and outboard by a 360° oil—lubricated, cylindrical bearing with 1.5" diameter and 6—mil radial clearance. The lubricant was T10 oil with 5 psi inlet pressure. The rotor was driven by 0.5 hp electric motor through a flexible coupling. Four orthogonal springs supported the outboard end of the shaft, in order to maintain concentric position of the journal inside the bearing at rest. The rotor carried some amount of unbalance.

The sets of XY proximity transducers were located at the fluid—lubricated bearing and at four other axial locations of the shaft (Figs. 5 and 6). The vibrational data from these transducers, as well as from the Keyphasor® (once per rotation pulse) transducer, were collected by the computerised data acquisition and processing system.

4.2 Experimental Results

Two cases with different positions of the disks on the shaft were investigated (Figs. 5 and 6). The rotor vibrational responses at specific rotative speeds were filtered to whirl or to whip

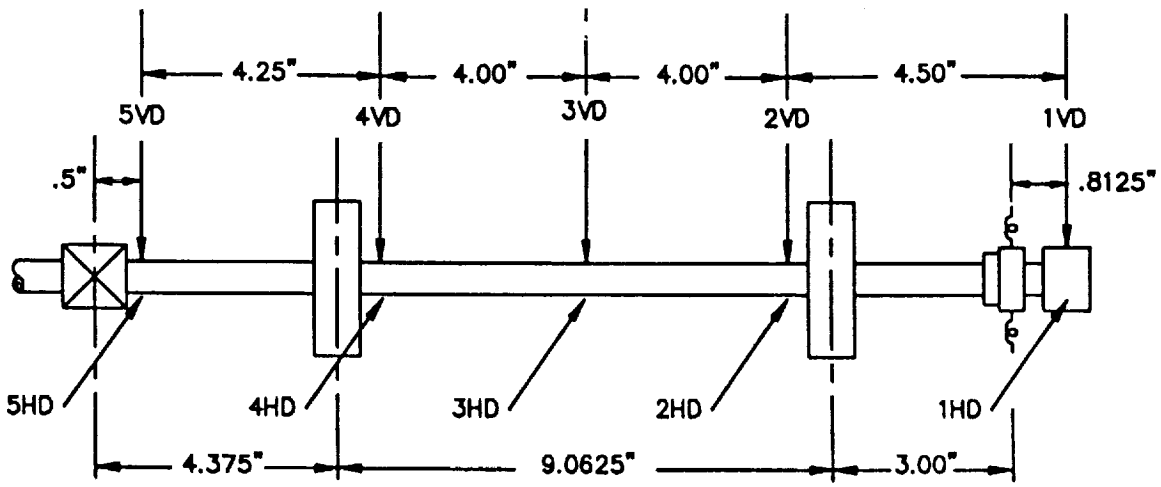

FIRST MODE WHIRL: Ω = 2440 rpm, ω_1 = 1170 cpm

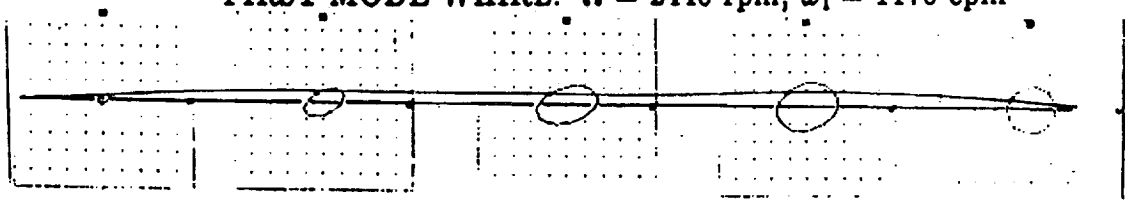

FIRST MODE WHIP: Ω = 3800 rpm, ω_2 = 1700 cpm

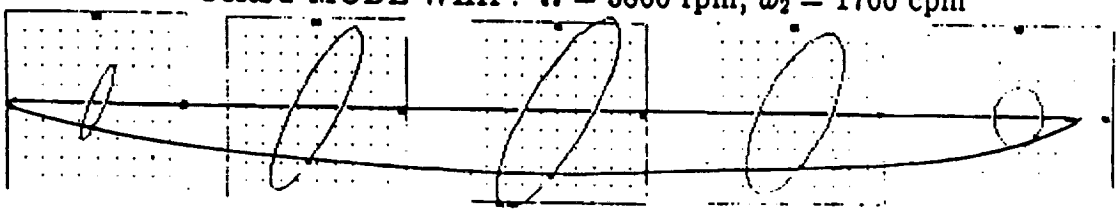

SECOND MODE WHIRL: Ω = 8800 rpm, ω_1 = 4200 cpm

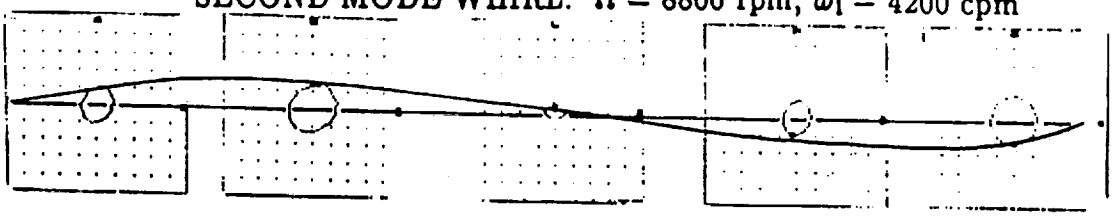

SECOND MODE WHIRL: Ω = 9200 rpm, ω_1 = 4220 cpm
(TRANSITION TO SECOND MODE WHIP)

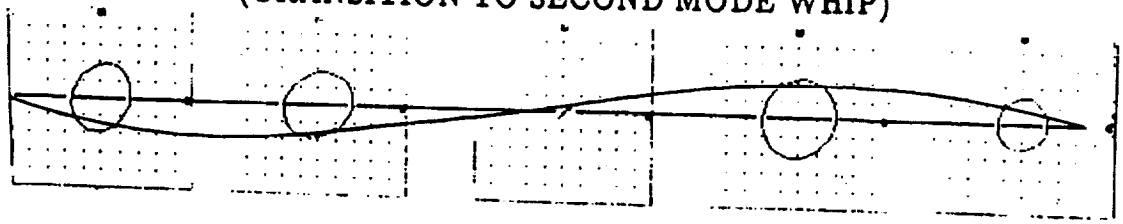

Fig. 5 Rotor sketch and rotor modal centerlines at the first and second mode whirl, the first mode whip, and at the transition from the second mode whirl to the second mode whip at specific rotative speeds. The orbits are filtered to whirl or whip frequencies ω_i, i=1,2. Orbit scale: 5 mil/div. Case 1: disks apart.

frequencies. The artificial Keyphasor marker positions were used to plot rotor centerline deflections for particular modes (Figs. 5 and 6). Figures 7 to 10 present the spectrum cascade plots during the rotor start–up. They exhibit synchronous (1×) unbalance–related vibrations and high rotor subsynchronous vibrations of the first and second mode whirl and of the whip type. Moving the disks toward the rotor midspan (case 2) resulted in a lowering the first natural frequency, and increasing the second one as compared with case 1. The first onset of instability occurred higher in case 2, but the second one occurred at a lower rotative speed. In both considered cases, rotor first mode whip vibration amplitudes were much higher than in the whirl modes. In both cases, the whip cessations occurred simultaneously with the second mode whirl onsets, but this is not a rule for other systems [9].

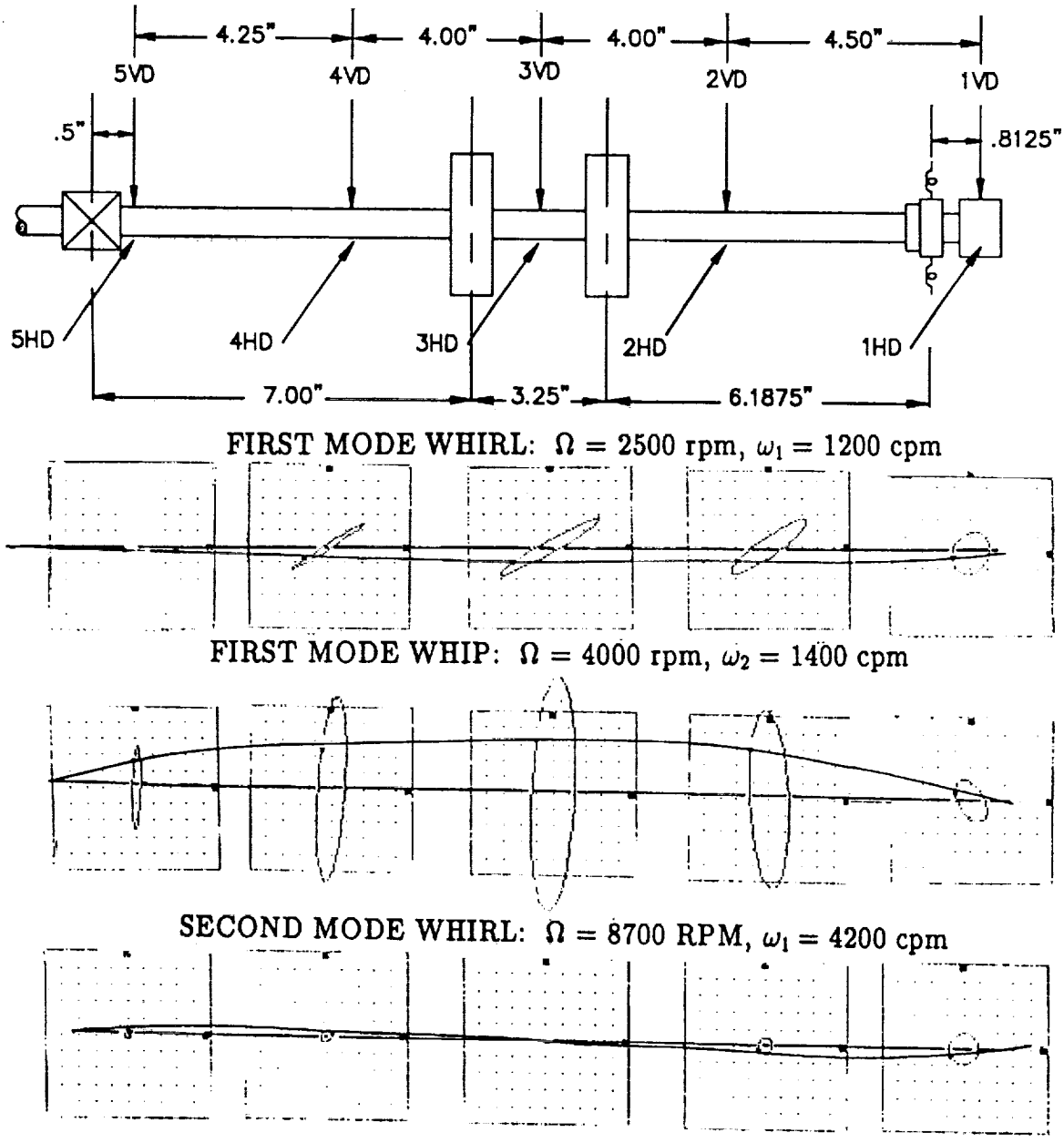

Fig. 6 Rotor sketch and rotor modal centerlines at the first and second mode whirl and at whip at specific rotative speeds. The orbits are filtered to whirl or whip frequencies ω_i, i=1,2. Orbit scale: 5 mil/div. Case 2: disks close to mid-span.

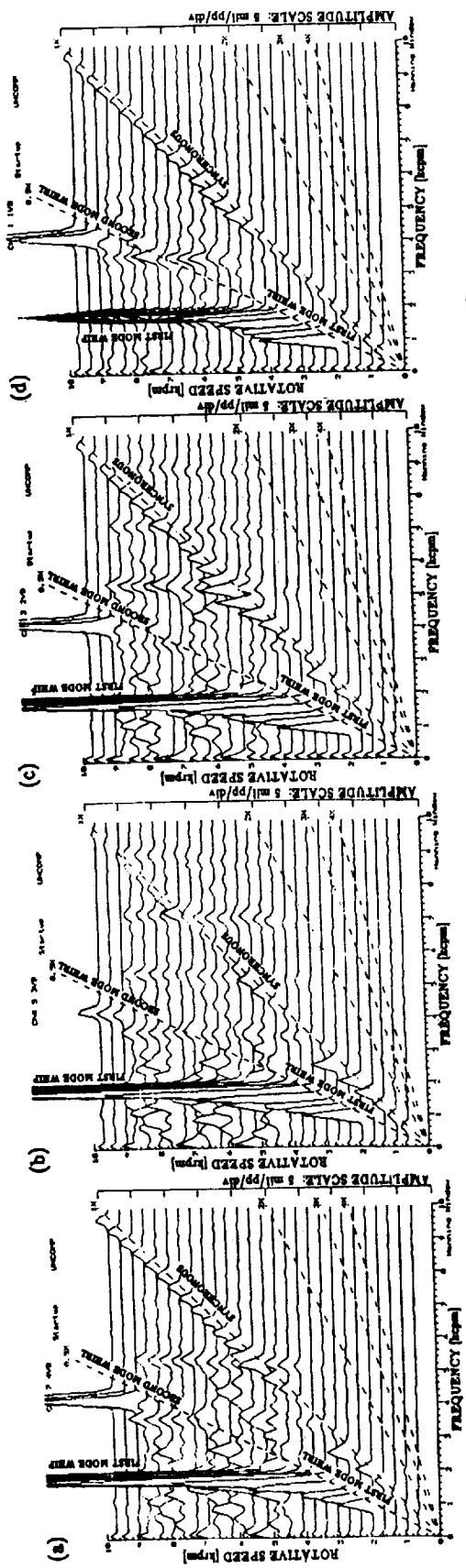

Fig. 7 Spectrum cascade plots of the rotor vertical responses during start-up, measured by the probes at axial locations 4(a), 3(b), 2(c), and 1 (journal) (d). Case 1.

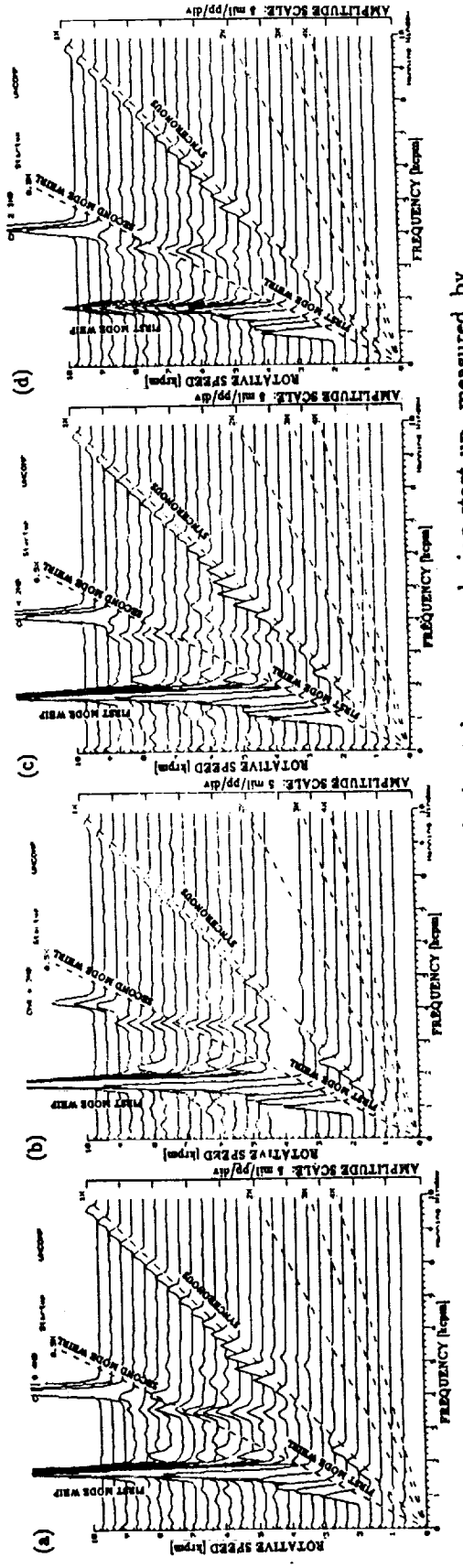

Fig. 8 Spectrum cascade plots of the rotor horizontal responses during start-up, measured by the probes at axial locations 4(a), 3(b), 2(c), and 1 (journal) (d). Case 1.

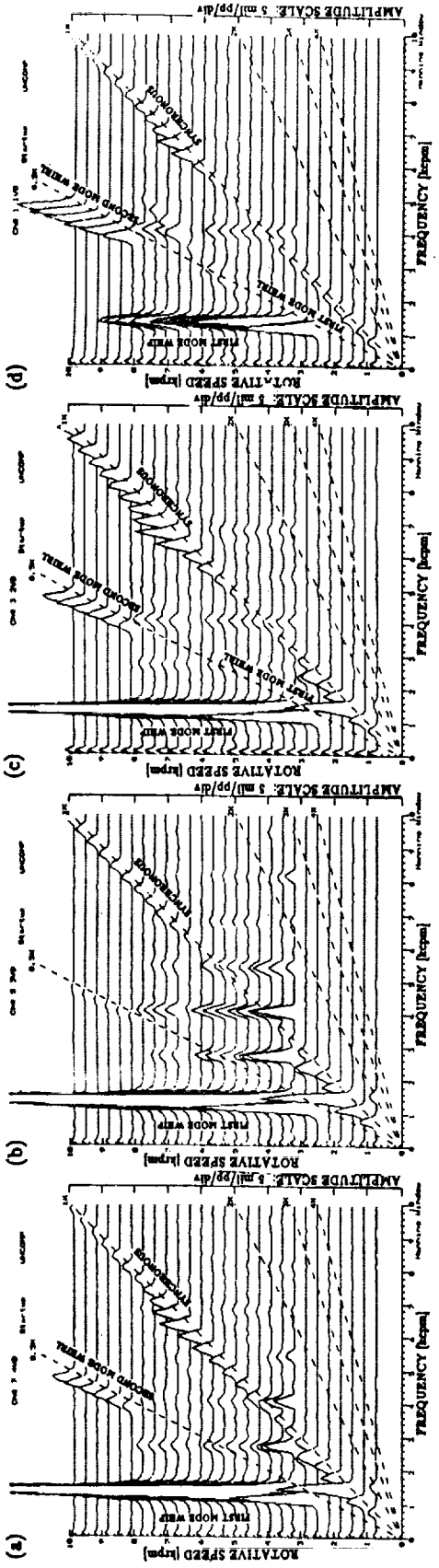

Fig. 9 Spectrum cascade plots of the rotor vertical responses during start-up, measured by the probes at vertical locations 4(a), 3(b), 2(c), and 1 (journal) (d). Case 2.

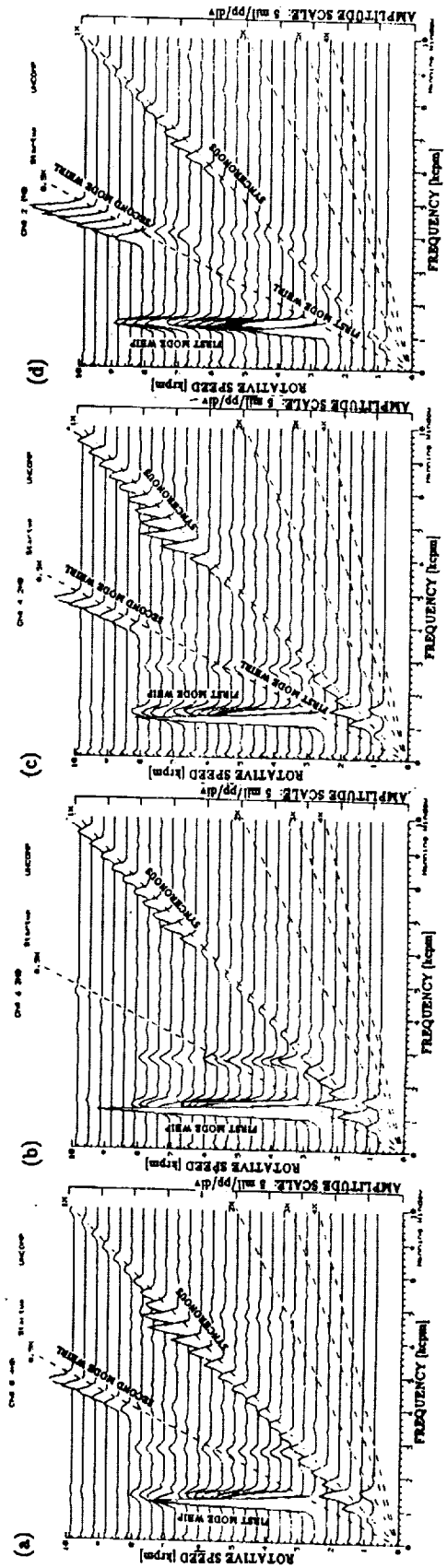

Fig. 10 Spectrum cascade plots of the rotor horizontal responses during start-up, measured by the probes at horizontal locations 4(a), 3(b), 2(c), and 1 (journal) (d). Case 2.

The modal parameter ratios as functions of the square root of mass ratio calculated from Eqs. (20) are presented in Figure 11. Since the modal parameter ratios must be positive, there exist limited ranges of mass ratios which satisfy this condition. It can be seen in Figure 11 that for case 1: $1.92 < \mu < 10.8$, and for case 2: $1.98 < \mu < 19.9$.

Perturbation testing should provide more reliable identification data [17].

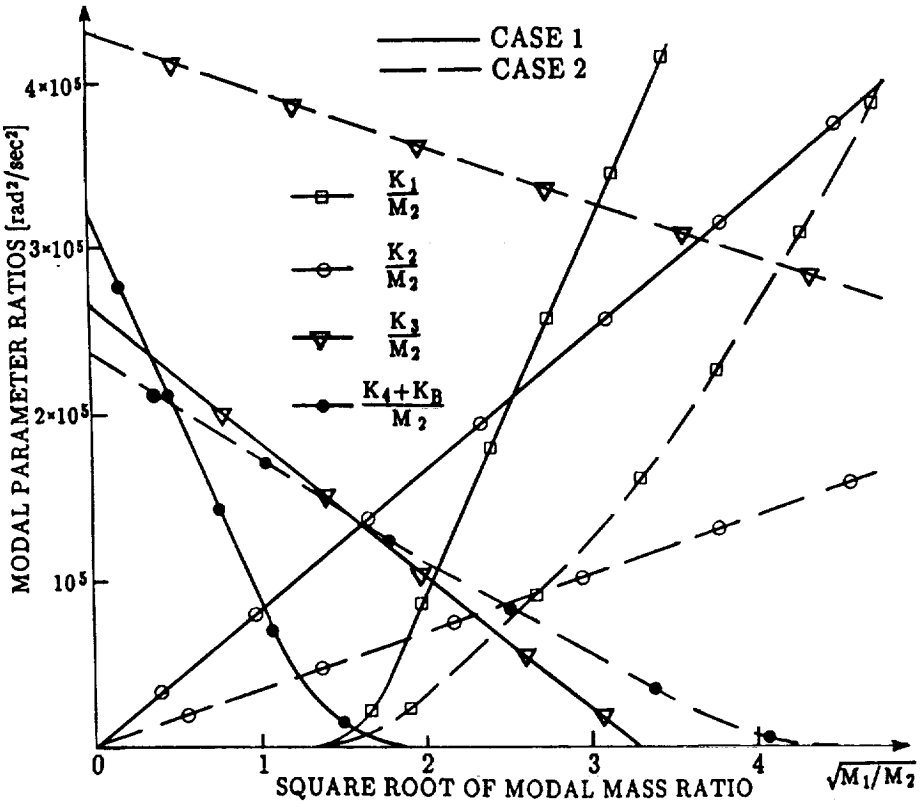

Fig. 11 Rotor modal parameter ratios as functions of the square foot of modal mass ratio.

NOTATION

A_i, α_i	Amplitudes and phases of rotor self-excited vibrations, respectively	$\bar{\kappa}_i, \kappa_i$	Rotor complex dynamic stiffnesses and their real parts, respectively
D, K_B	Fluid radial damping and radial stiffness, respectively	λ	Fluid circumferential average velocity ratio
$z_i, \lvert z_i \rvert$	Rotor complex lateral displacements and their absolute values	$\mu = M_1/M_2$	Modal mass ratio
		$\bar{\phi}_{i\nu}$	Rotor complex modal functions
D_i, M_i	Rotor modal damping coefficients and modal masses, respectively	ψ	Fluid nonlinear stiffness function
K_i	Rotor modal stiffnesses	ω	Complex eigenvalue; also self-excited vibration frequency
i, ν	Integers	ω_i	Approximate natural frequencies of the rotor system
$j = \sqrt{-1}$			
t	Time	ω_{ni}	Rotor natural frequencies
x_i, y_i	Rotor horizontal and vertical displacements, respectively	Ω	Rotative speed
		$\Omega_{ST\,i}$	Thresholds of stability

REFERENCES

1. Kirk, R. G., Nicholas, J. C., Donald, G. H., and Murphy, R. C., Analysis and Identification of Synchronous Vibration for a High Pressure Parallel Flow Centrifugal Compressor, Rotordynamic Instability Problems in High Performance Turbomachinery, NASA CP 2133, College Station, Texas, 1980.
2. Doyle, H. E., Field Experiences With Rotor Dynamic Instability in High Performance Turbomachinery, Rotordynamic Instability Problems in High—Performance Turbomachinery, NASA CP 2133, College Station, Texas, 1980.
3. Wachel, J. C., Rotordynamic Instability Field Problems, Rotordynamic Instability Problems in High Performance Turbomachinery, NASA CP 2250, College Station, Texas, 1982.
4. Baxter, N. L., Case Studies of Rotor Instability in the Utility Industry, Rotor Dynamical Instability, AMD, v. 55, New York, 1983.
5. Schmied, J., Rotordynamic Stability Problems and Solutions in High Pressure Turbocompressors, Rotordynamic Instability Problems in High Performance Turbomachinery, NASA CP 3026, College Station, Texas, 1988.
6. Laws, C. W., Turbine Instabilities—Case Histories, Instability in Rotating Machinery, NASA CP 2409, Carson City, Nevada, 1985.
7. Muszynska, A., Whirl and Whip — Rotor/Bearing Stability Problems, Journal of Sound and Vibration, v. 110, No. 3, 1986.
8. Muszynska, A., Multi—Mode Whirl and Whip in Rotor/Bearing Systems, Dynamics of Rotating Machinery, The Second International Symposium on Transport Phenomena, Dynamics, and Design of Rotating Machinery, v. 2, Hemisphere Publ. Corp., Honolulu, Hawaii, 1988.
9. Muszynska, A., Grant, J. W., Stability and Instability of a Two—Mode Rotor Supported by Two Fluid—Lubricated Bearings, Trans. ASME Journ. of Vibration and Acoustics, v. 113, No. 3, 1991.
10. Muszynska, A., The Role of Flow—Related Tangential Forces in Rotor/Bearing Seal System Stability, ISROMAC—3, Honolulu, Hawaii, 1990.
11. Bently, D. E. and Muszynska, A., Anti—Swirl Arrangements Prevent Rotor/Seal Instability, Trans. ASME Journal of Vibration, Acoustics, Stress and Reliability in Design, v. 111, No. 2, 1989.
12. Bolotin, V. V., Nonconservative Problems in Theory of Elastic Stability, The MacMillan Company, New York, 1963.
13. Black, H. G., Effects of Hydraulic Forces in Annular Pressure Seals on the Vibrations of Centrifugal Pump Rotors, Journal of Mechanical Engineering Science, v. II, No. 2, 1969.
14. Black, H. F., Jensen, D. N., Dynamic Hybrid Bearing Characteristics of Annular Controlled Leakage Seals, Proceedings Journal of Mechanical Engineering, v. 184, 1970.
15. Muszynska, A., Improvements in Lightly Loaded Rotor/Bearing and Rotor/Seal Models, Trans. ASME, Journal of Vibration, Acoustics, Stress and Reliability in Design, v. 110, No. 2., pp. 129—136, 1988.
16. Muszynska, A., Modal Testing of Rotor/Bearing Systems, The International Journal of Analytical and Experimental Modal Analysis, v. 1, No. 3, 1986.
17. Muszynska, A., Perturbation Technique for Identification of the Lowest Modes of Rotors With Fluid Interaction, Proc. of the Course on "Rotor Dynamics and Vibration in Turbomachinery," von Karman Institute for Fluid Dynamics, Belgium, September 1992.
18. Bently, D. E., Bosmans, R. F., A Method to Locate the Source of a Rotor Fluid—Induced Instability Along the Rotor, ISROMAC—3, Honolulu, Hawaii, 1990.

During whip conditions the whip frequency filtered orbits are elliptical, reflecting rotor system anisotropic features. During whirl conditions the orbits are circular (except the first-mode whirl in case 2), and much smaller than at whips (Figs. 5, 6). There exist higher harmonic and combinational components in the spectra (Figs. 7 to 10), especially when amplitudes of whip vibrations are high (Figs. 7, 8) causing involvement of geometric nonlinearities.

The first instability onset in case 2 (Figs. 9, 10) occurs at relatively high rotative speed, in the range of the transition to whip rather than at whirl, as in case 1 (Figs. 7, 8). The phases and amplitudes of these self-excited vibrations change considerably just after the onset: first the horizontal amplitudes are large, then, at higher rotative speed, in whip conditions, the vertical amplitudes become dominant (Fig. 9).

4.3 Identification of Rotor Modal Parameters From Experimental Results

In this section a method of partial (incomplete) identification of the rotor two-mode modal parameters will be outlined. This method does not pretend to be general; the identification results show only that the modal modelling is feasible, simple, and reflects major dynamic features of the rotor behavior.

The data for identification is taken from the start-up runs (Figs. 7 to 10): rotor natural frequencies of the first two modes, ω_{n1}, ω_{n2}, and the onsets of instability for the first and second mode whirls, $\Omega_{ST\,1}$, $\Omega_{ST\,2}$. From Eqs. (9) and (10), the rotor parameters are calculated as follows:

$$\frac{K_2}{M_2} = [b(\omega_{n1}^2 + \omega_{n2}^2 - b) - \omega_{n1}^2\omega_{n2}^2]\sqrt{\mu}\,, \qquad \frac{K_1}{M_2} = b\mu - \frac{K_2}{M_2} \tag{20}$$

$$\frac{K_3}{M_2} = \omega_{n1}^2 + \omega_{n2}^2 - b - \frac{K_2}{M_2}\,, \qquad \frac{K_B+K_4}{M_2} = \frac{K_3}{M_2}\left[\frac{K_3/M_2}{\omega_{n1}^2+\omega_{n2}^2-\lambda^2(\Omega_{ST\,1}^2+\Omega_{ST\,2}^2)} - 1\right]$$

where

$$b = \frac{\omega_{n1}^2\omega_{n2}^2 - \lambda^4\,\Omega_{ST\,1}^2\,\Omega_{ST\,2}^2}{\omega_{n1}^2 + \omega_{n2}^2 - \lambda^2(\Omega_{ST\,1}^2 + \Omega_{ST\,2}^2)}\,, \qquad \mu = \frac{M_1}{M_2}$$

Since there are only four equations, (9) and (10), and seven unknown parameters, the stiffness-to-mass ratios are expressed as functions of the modal mass ratio μ.

The data for the cases 1 and 2 are given in Table 1.

TABLE 1. Experimental Data

	ω_{n1}	ω_{n2}	$\Omega_{ST\,1}$	$\Omega_{ST\,2}$	λ
	rpm				—
Case 1	1677	5200	2000	8800	0.48
Case 2	1400	6300	2500	8000	0.48